Table 62. Skew scattering (ϕ) and side jump (ΔL) contributions to the anomalous Hall effect [87O3].

	ϕ	ΔL [Å]
NiMnSb	– 0.037°	0.48
PtMnSb	– 0.017°	0.43
AuMnSb	– 0.76°	0.56
CoMnSb	1.1°	0.08
PtMnSn	1.2°	0.14

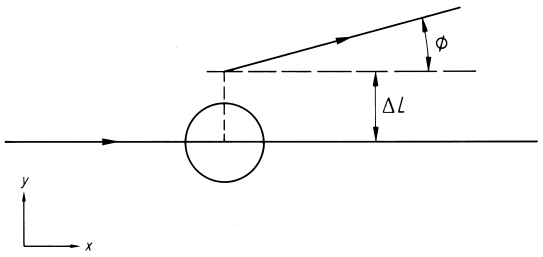

Fig. 312. Asymmetric scattering of charge carriers with spin up, due to skew scattering ϕ and side jump ΔL. For an electron with spin down $\phi \rightarrow -\phi$ and $\Delta L \rightarrow -\Delta L$. The spin up and down directions refer to the *z* axis [87O3].

1.5.5.6.3 Superconductivity

Superconductivity in Heusler alloys has primarily focused on compounds containing lanthanide elements. However, there have been some limited reports on transition metal compounds.

X_2YZ X = 3d, Y = 4d

X = 8A: Ni
Y = 5A: Nb
Z = 3B: Al, Ga; 4B: Sn

Ni_2NbZ

Critical temperatures up to 2.9 K were reported for compounds in this series which have been classified as intermediate coupled systems.

Interest in Heusler alloys containing rare earth elements arose from the possibility of the co-existence of long-range magnetic order and superconductivity [85J3]. The fact that they readily form a single phase $L2_1$ structure also made them attractive. It is thought that the co-existence of superconductivity and magnetic order arises from the relative weakness of the exchange spin flip (pair breaking) interaction between the closed 4f shells of the magnetic atoms and the conduction electrons. A possible source of complication is the degree of atomic order which is often not specified but is known to affect the magnetic properties.

Table 63. A summary of the lattice constant, superconducting transition temperature T_c, electronic specific heat coefficient γ, Debye temperature Θ_D, electron - phonon coupling constant λ, upper critical field H_{c2} for Ni_2NbZ alloys with Z = Al, Ga or Sn [85W1].

Compound	a [Å]	T_C [K]	γ [mJ mol^{-1} K^{-2}]	Θ_D [K]	λ	$H_{c2}(0)$ [kOe]	$-(dH_{c2}/dT)_{Tc}$ [kOe K^{-1}]
Ni_2NbAl	5.969	2.15	8.0	280	0.52	≈ 13.5	6.5
Ni_2NbGa	5.956	1.54	6.5	240	0.50	≈ 6.0	6.4
Ni_2NbSn	6.157	2.90	4.0	206	0.61	≈ 6.3	3.7

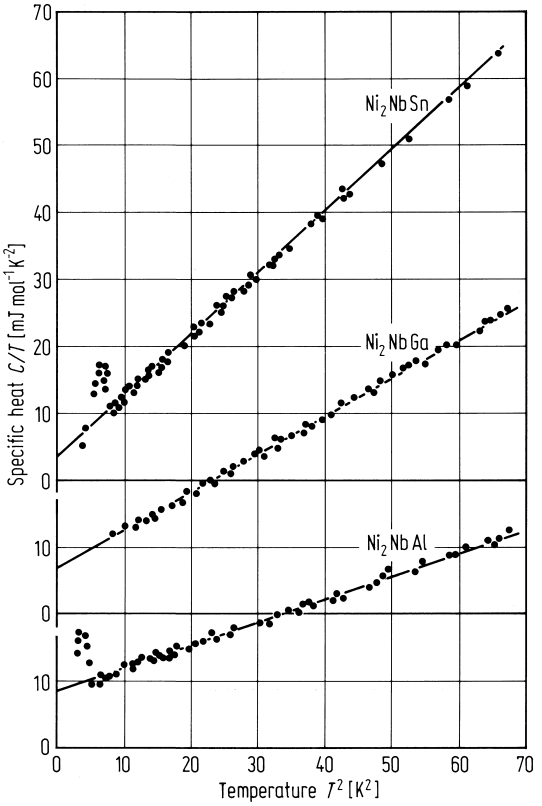

Fig. 313. Specific heat of Ni_2NbZ alloys with Z = Al, Ga or Sn. The solid lines indicate a least squares fit of the formula $C(T) = \gamma T + \beta T^3$ to the data [85W1].

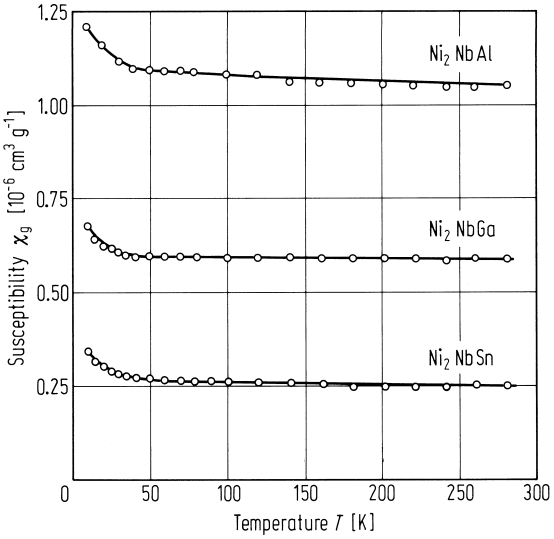

Fig. 314. Temperature dependence of the magnetic susceptibility of Ni_2NbZ (Z = Al, Ga, Sn) [85W1].

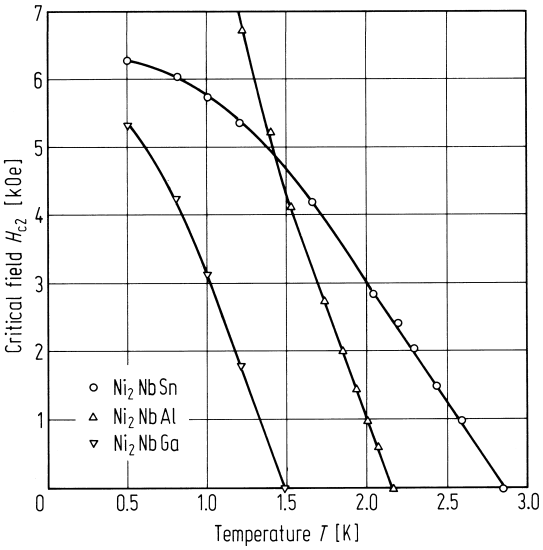

Fig. 315. Upper critical field H_{c2} vs. temperature for Ni_2NbZ for Z = Al, Ga, Sn [85W1].

X_2YZ X = 4d, Y = 3d, 4d, 4f

X = 8A: Pd
Y = 3A: Sc, Y; 4A: Gd, Dy, Ho, Er, Tm, Yb
Z = 4B: Sn

Pd_2YSn

The compound Pd_2YSn orders in the $L2_1$ structure and becomes superconducting below 4.55 K. The effect on T_c of replacing Y by a rare earth element is to depress T_c with the largest effect caused by Gd. The initial rate of depression of T_c deviation is determined from the de Gennes function $(g_J - J)^2 J(J + 1)$ [85M2].

Table 64. A summary of the compositional dependence of lattice parameter and superconducting transition temperature in Pd_2YSn alloys [85J3].

Composition [at%]			a [Å]	T_c [K]
Pd	Y	Sn		
48	26	26	6.722(2)	5.2
50	29	21	6.700(1)	2.70
50	28	22	6.711(2)	3.65
50	26	24	6.713(1)	4.0
50	25	25	6.702(1)	3.50
50	24	26	6.718(3)	5.20
51	27	22	6.708(2)	
51	25	24	6.721(2)	5.20
51	24	25	6.720(1)	5.0
52	26	22	6.716(3)	5
52	25	23	6.717(1)	4.6
52	24	24	6.718(3)	5.5
53	24	23	6.718(2)	5
53	23	24	6.717(2)	5

Table 66. Experimentally estimated and / or scaled crystalline electric field parameters for various rare earth ions in Pd_2RSn compounds. For cubic symmetry $B_4^4 = 5B_4^0$ and $B_6^4 = -21B_6^0$. The ground state, the first excited state and their energy separation (in K) are also given [85M2].

R	B_4^0 [10^{-2} K]	B_6^0 [10^{-4} K]	Ground state	First excited state [at energy in K]
Dy	– 0.61	0.38	Γ_7	$\Gamma_6(26)$
Ho	0.32	0.41	$\Gamma_5^{(1)}$	$\Gamma_3^{(1)}(112)$
Er	– 0.39	– 0.60	$\Gamma_8^{(3)}$	$\Gamma_6(215)$
Tm	– 0.014	1.48	$\Gamma_5^{(1)}$	$\Gamma_3(28)$
Yb	0.13	– 33.0	Γ_7	$\Gamma_8(38)$

Table 65. Lattice parameter a and superconducting transition temperature T_c of Pd_2ScSn, Pd_2LuSn and $Pd_2Y_{1-x}R_xSn$ alloys for different rare earth metals and for various values of x [85M2].

Compound	a [Å]	T_c [K]
Pd_2ScSn	6.503	2.05
Pd_2LuSn	6.644	3.05
Pd_2YSn	6.716	4.55
$Pd_2Y_{0.98}Gd_{0.02}Sn$	6.716	3.24
$Pd_2Y_{0.95}Gd_{0.05}Sn$	6.717	2.41
$Pd_2Y_{0.9}Gd_{0.1}Sn$	6.722	[a])
$Pd_2Y_{0.9}Dy_{0.1}Sn$	6.716	3.46
$Pd_2Y_{0.85}Dy_{0.15}Sn$	6.718	2.80
$Pd_2Y_{0.8}Dy_{0.2}Sn$	6.718	1.40
$Pd_2Y_{0.7}Dy_{0.3}Sn$	6.722	[a])
$Pd_2Y_{0.9}Ho_{0.1}Sn$	6.715	4.06
$Pd_2Y_{0.9}Er_{0.1}Sn$	6.715	3.87
$Pd_2Y_{0.8}Er_{0.2}Sn$	6.714	3.73
$Pd_2Y_{0.7}Er_{0.3}Sn$	6.714	3.80
$Pd_2Y_{0.6}Er_{0.4}Sn$	6.711	2.77
$Pd_2Y_{0.95}Tm_{0.05}Sn$	6.716	4.12
$Pd_2Y_{0.9}Tm_{0.1}Sn$	6.710	4.12
$Pd_2Y_{0.75}Tm_{0.25}Sn$	6.703	3.73
$Pd_2Y_{0.5}Tm_{0.5}Sn$	6.690	3.65
$Pd_2Y_{0.25}Tm_{0.75}Sn$	6.681	3.06
Pd_2TmSn	6.670	2.82
$Pd_2Y_{0.9}Yb_{0.1}Sn$	6.713	4.37
$Pd_2Y_{0.7}Yb_{0.3}Sn$	6.704	4.03
Pd_2YbSn	6.658	2.42

[a]) No superconducting transition down to 1.2 K.

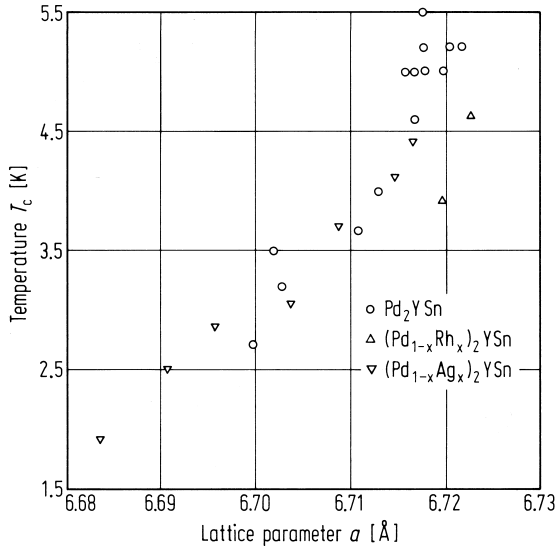

Fig. 316. Dependence of the lattice parameter and superconducting transition temperature T_c on the nominal composition of Pd_2YSn [85J3].

Table 67. Values of $N(0)\cdot J_{sf}^2$ obtained from the suppression of T_c data in $Pd_2Y_{1-x}R_xSn$ (a) for free rare earth ions, (b) with crystalline electric fields and (c) with crystalline electric fields and different T_{c0} for different concentrations. The error based on experimental results is ± 20 % [85M2].

Impurity	$N(0)\cdot J_{sf}^2$ [10^{-4} eV]		
	(a)	(b)	(c)
Gd	1.83	1.83	1.83
Dy	1.23	2.29	2.29
Ho	0.75	1.21	1.21
Er	1.15	1.64	1.64
Tm	1.18	2.08	1.04
Yb	4.48	6.77	3.23

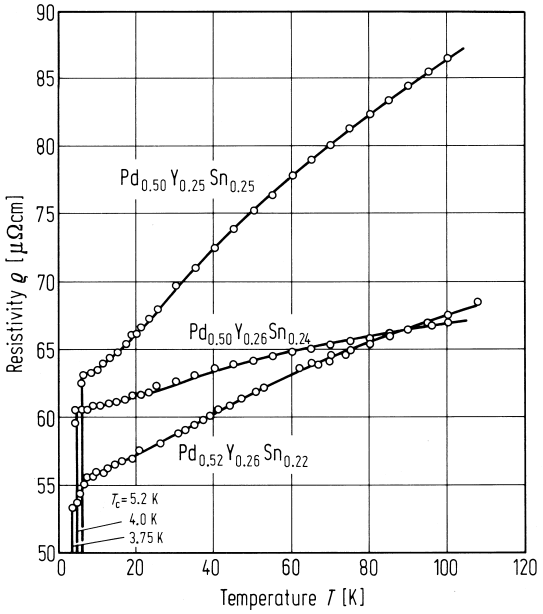

Fig. 317. Electrical resistivity of three compounds of Pd_2YSn around the stoichiometric composition. The transition temperatures associated with the onset of superconductivity are shown in the figure [85J3].

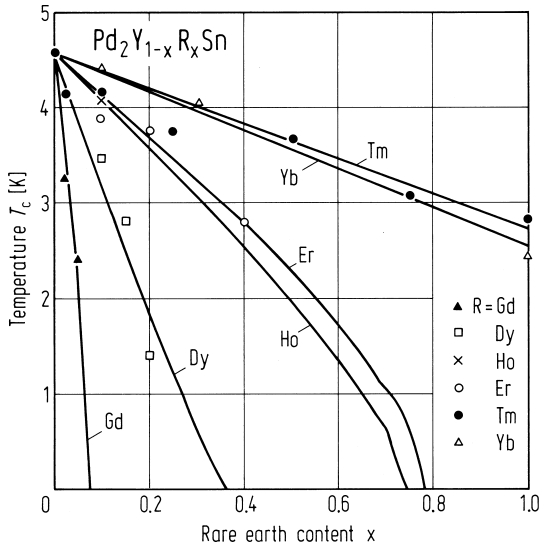

Fig. 318. Variation of the superconducting transition temperature as a function of the rare earth concentration x in $Pd_2Y_{1-x}R_xSn$ (R = Gd, Dy, Ho, Er, Tm, Yb). The solid lines are fits to the data based on the Abrikosov-Gorkov theory and including the effects of CEF. (see Table 66) [85M2].

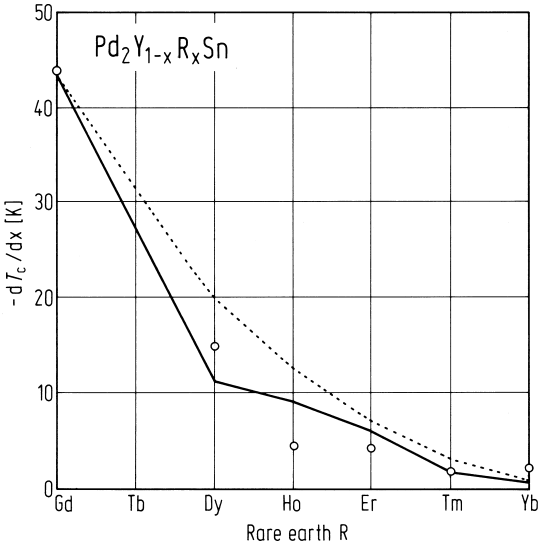

Fig. 319. Initial suppression of T_c with x ($-\mathrm{d}T_c/\mathrm{d}x$) as a function of rare earth ion in $Pd_2Y_{1-x}R_xSn$ (R = Gd, Dy, Ho, Er, Tm, Yb) compounds. The dotted line is based on the de Gennes function after re-normalising to the value for Gd. The solid line is based on the Abrikosov-Gorkov theory with the inclusion of CEF effects and with $N(0)\cdot J_{sf}^2 = 1.83\cdot 10^{-4}\,\mathrm{eV}$, the value derived for the Gd substituted system [85M2].

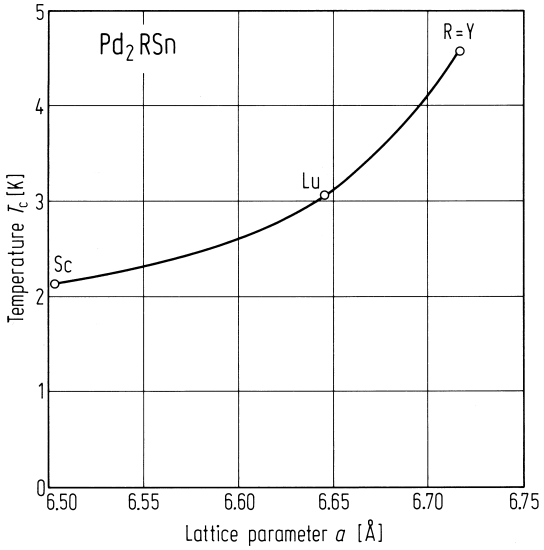

Fig. 320. Superconducting transition temperature vs. lattice parameter for Pd_2RSn (R = Sc, Lu, Y) compounds [85M2].

Re-entrant behaviour

$Pd_2Y_{1-x}Dy_xSn$

Superconductivity is completely suppressed at a critical Dy concentration of x ≈ 0.35. Samples with x ≥ 0.5 order antiferromagnetically. The superconducting samples with x ≤ 0 show re-entrant behaviour under external applied fields.

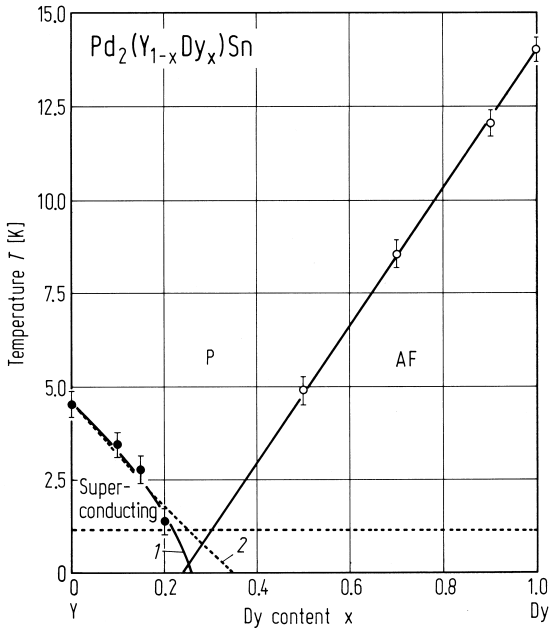

Fig. 321. Superconducting and magnetic phase diagram of the Heusler alloy system $Pd_2Y_{1-x}Dy_xSn$ as determined from ac susceptibility measurements. On the superconducting side the curve labelled (*1*) is obtained from the Abrikosov-Gorkov (AG) type of analysis with the neglect of crystalline electric field (CEF) effects and with $N(0)\cdot J_{sf}^2 = 1.23\cdot 10^{-4}$eV, curve (*2*) is obtained from an AG-type analysis with the inclusion of CEF effects and with $N(0)\cdot J_{sf}^2 = 2.29\cdot 10^{-4}$eV.
The dashed line at 1.2 K parallel to the temperature axis represents the lower limit down to which ac susceptibility measurements have been carried out on all these samples [86M2].

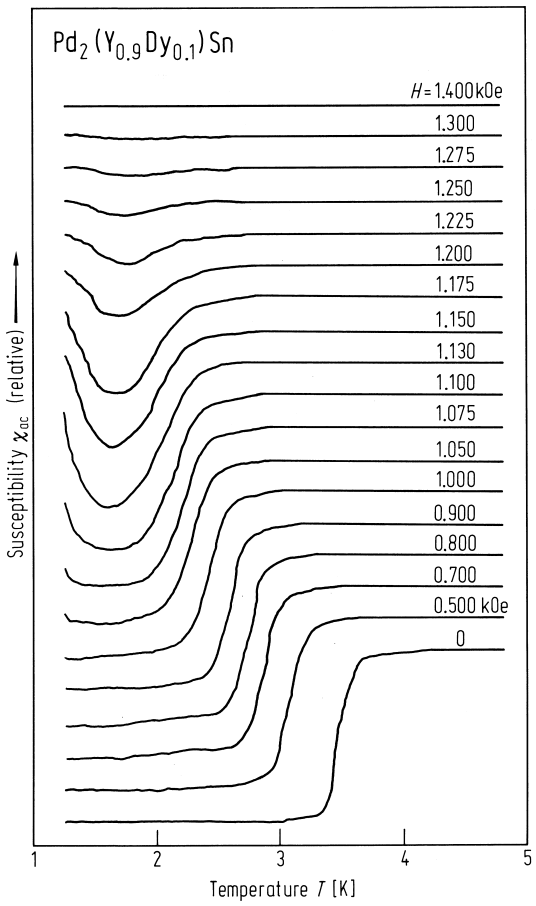

Fig. 322. Plot of the ac susceptibility χ_{ac} vs. temperature in $Pd_2Y_{0.9}Dy_{0.1}Sn$ showing the field induced re-entrant behaviour [86M2].

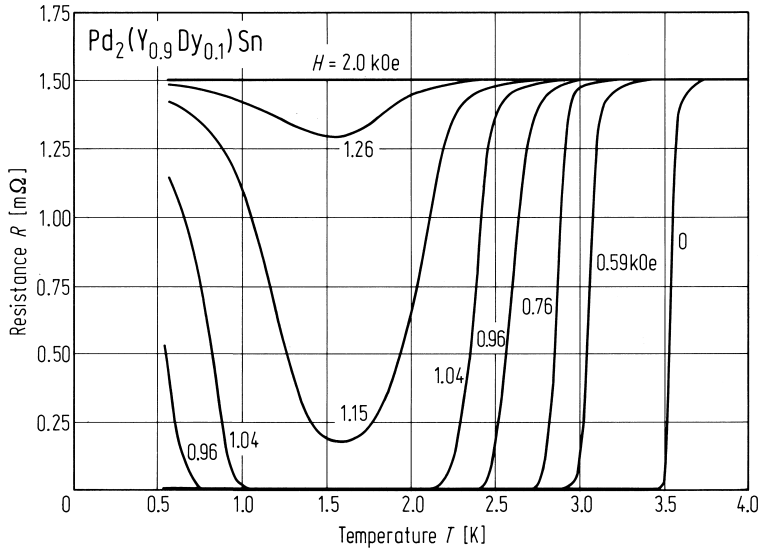

Fig. 323. Variation of electrical resistance vs. temperature in various applied fields for $Pd_2Y_{0.9}Dy_{0.1}Sn$ showing the transition into a re-entrant state [86M2].

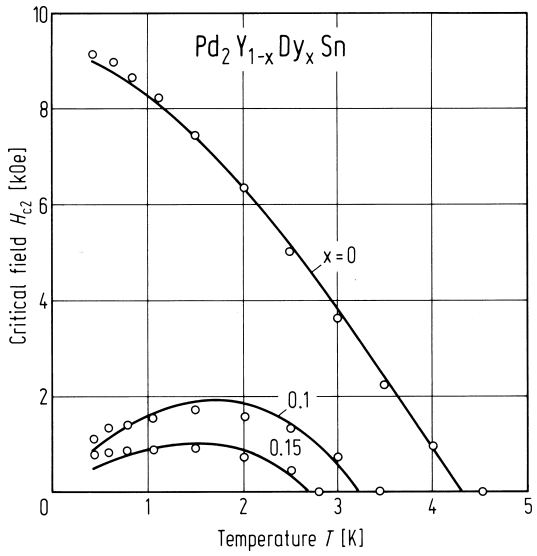

Fig. 324. Temperature dependence of the upper critical field H_{c2} in $Pd_2Y_{1-x}Dy_xSn$ (x = 0.0, 0.1, 0.15) compounds. The solid lines are the fits to the data based on the WHH theory including pair-breaking effects due to magnetic ions [86M2].

Co-existence of magnetism and superconductivity

Pd_2ErSn

The co-existence of long-range magnetic order and superconductivity has been reported in Pd_2ErSn below ≈ 1 K. The compound becomes superconducting below 1.17 K and magnetic below 1.0 K, with the superconducting state being retained to at least 40 mK [86S1].

Table 68. A summary of lattice parameters and superconducting transition temperatures of $Pd_2(Y_xEr_{1-x})Sn$ alloys [86S1].

x	*a* [Å]	T_c [K]
0.00	6.6834(8)	1.17 – 0.89 [a])
		1.23 – 1.16 [b])
0.05	6.6864(8)	1.26 – 1.08 [a])
0.10	6.6873(6)	1.60 – 1.36 [a])
0.20	6.6890(8)	2.08 – 1.80 [a])
0.40	6.6973(6)	2.59 – 2.37 [a])
0.60	6.7024(8)	3.66 – 3.46 [a])
0.80	6.7096(8)	4.38 – 4.22 [a])
1.00	6.7165(8)	5.26 – 5.04 [a])

[a]) 10 – 90 % inductive transition.
[b]) 10 – 90 % resistive transition.

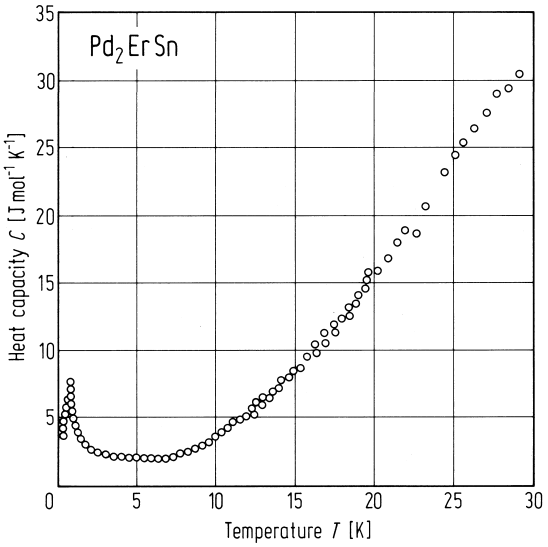

Fig. 325. Heat capacity as a function of temperature for Pd_2ErSn [86S1].

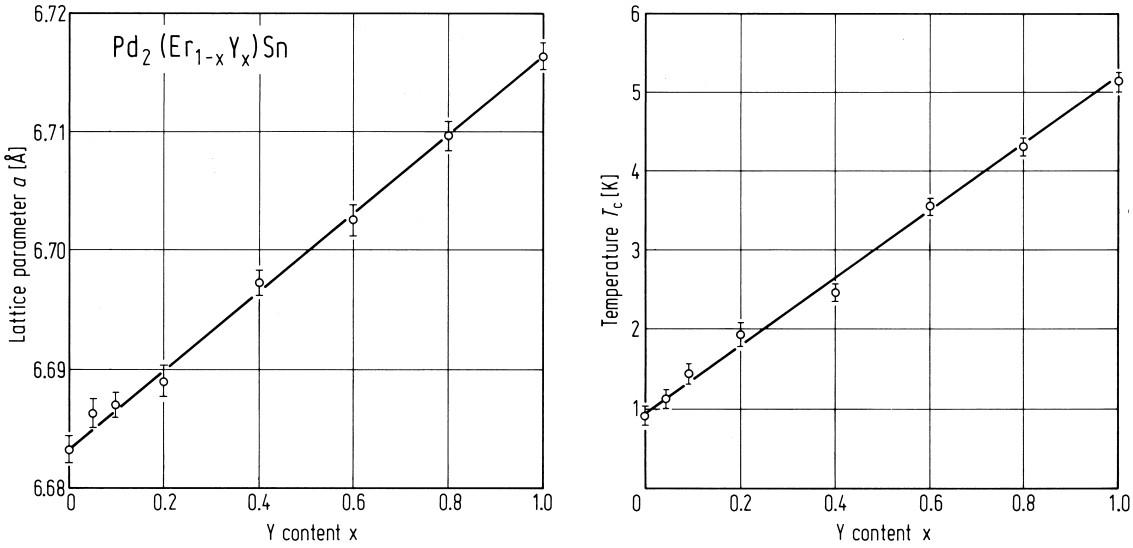

Fig. 327. Superconducting transition temperature T_c and cubic lattice parameter *a* for $Pd_2(Er_{1-x}Y_x)Sn$ alloys [86S1].

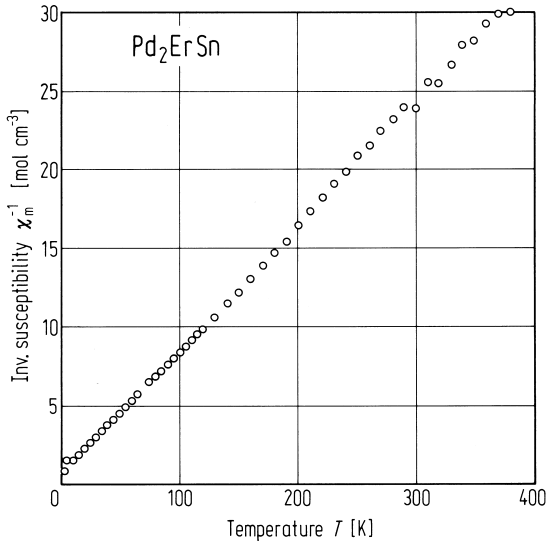

Fig. 326. Inverse magnetic molar susceptibility vs. temperature for Pd_2ErSn measured in a field of 0.2 T [86S1].

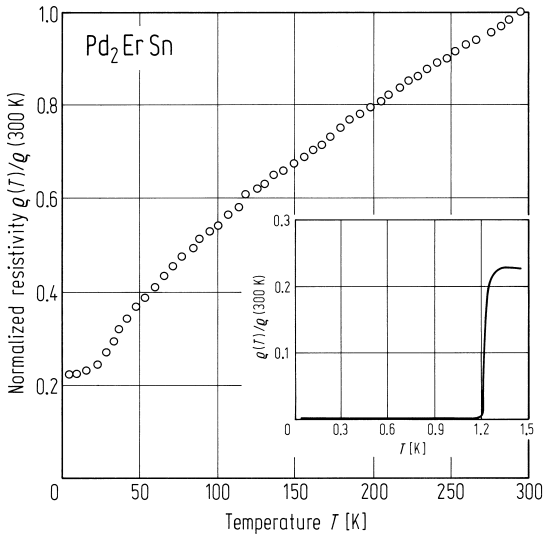

Fig. 328. Electrical resistivity normalised at 300 K for Pd_2ErSn. Inset shows the superconducting transition and the low-temperature limit of 40 mK [86S1].

Pd_2YbSn

The compound becomes superconducting below 2.46 K and magnetic below 0.23 K. The absence of re-entrant behaviour shows that the magnetically ordered state is co-existent with the superconductivity.

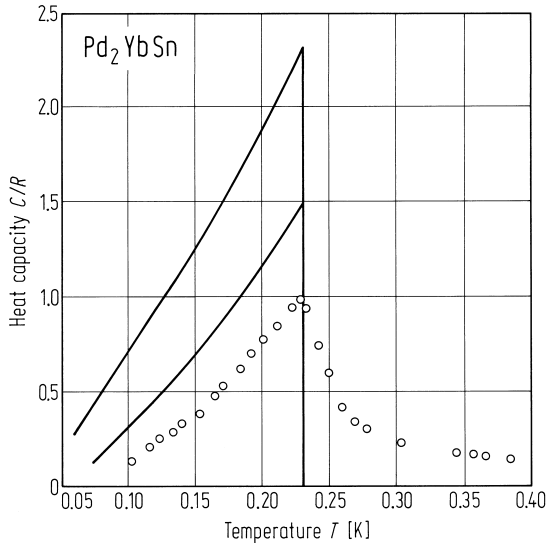

Fig. 330. Heat capacity of Pd_2YbSn showing the magnetic transition at 0.23 K. The upper solid curve shows the mean field heat capacity for a quartet crystal field ground state, and the lower solid curve for a doublet ground state [85K1].

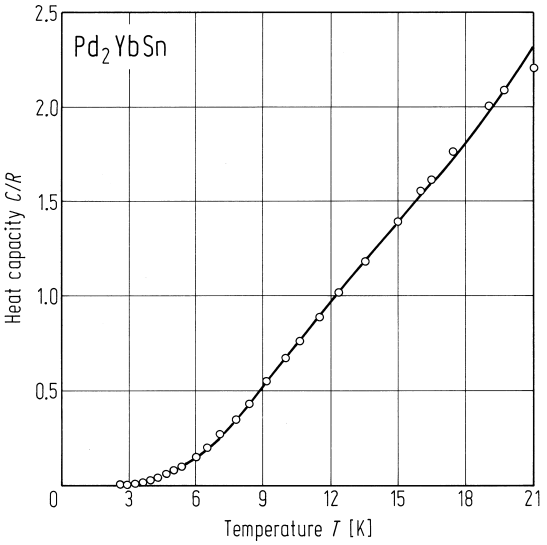

Fig. 331. Heat capacity of Pd_2YbSn in the region above the superconducting transition temperature. The solid curve is a fit to the data including contributions from the electronic heat capacity, the lattice heat capacity and the electronic Schottky effect from CEF levels [85K1].

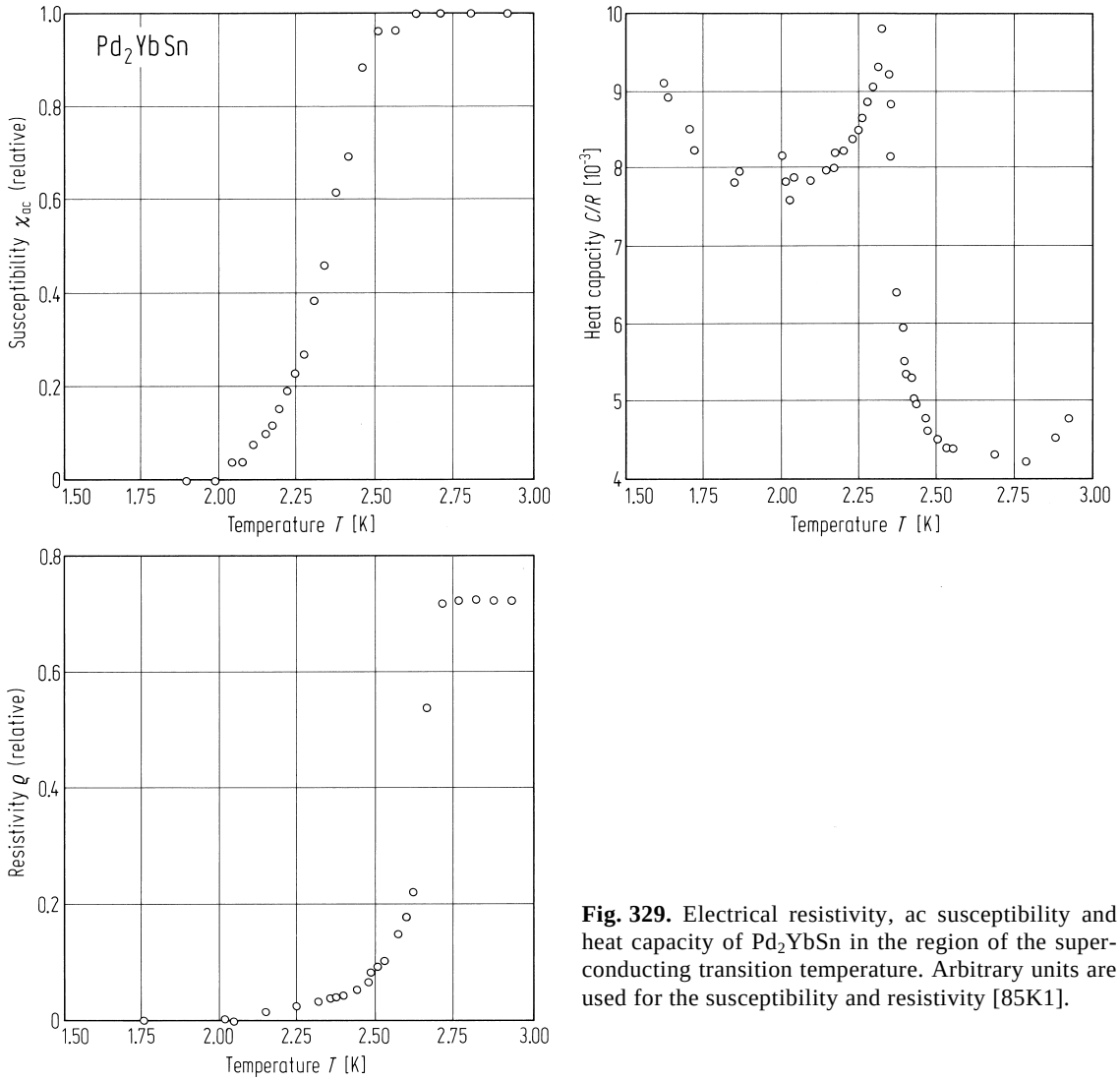

Fig. 329. Electrical resistivity, ac susceptibility and heat capacity of Pd_2YbSn in the region of the superconducting transition temperature. Arbitrary units are used for the susceptibility and resistivity [85K1].

Pressure dependence of T_C

The application of hydrostatic pressure up to 20 kbar linearly suppresses the transition temperature. This depression has been interpreted as arising from a stiffening of the Pd sublattice [84J1].

Table 69. A summary of the pressure dependence of the superconducting transition temperature T_c in Pd_2YSn alloys [84J1]. Θ_D: Debye temperature.

Compounds	a [Å]	T_c [a]) [K]	$-dT_c/dp$ [10^{-5} K/bar]	$-d\ln T_c/dp$ [10^{-6}/bar]	Θ_D [K]
$ScPd_2Sn$	6.509 ± 0.062	2.29 – 2.25 – 2.19	1.45 ± 0.10	6.44 ± 0.44	232
YPd_2Sn	6.719 ± 0.039	5.02 – 4.92 – 4.81	2.26 ± 0.21	4.61 ± 0.43	165 [b])
YPd_2Pb	6.786 ± 0.008	4.13 – 4.05 – 4.01	1.95 ± 0.15	4.81 ± 0.36	198 [b])
$TmPd_2Sn$	6.668 ± 0.003	1.92 – 1.77 – 1.52	2.62 ± 0.09	14.80 ± 0.54	120
$YbPd_2Sn$	6.657 ± 0.007	1.82 – 1.79 – 1.76	1.93 ± 0.09	10.92 ± 0.49	118
$LuPd_2Sn$	6.644 ± 0.004	3.02 – 2.98 – 2.75	1.68 ± 0.07	5.43 ± 0.22	118

[a]) 10 %-midpoint-90 % values at ambient pressure.
[b]) Determined from specific heat measurements by Ishikawa et al. Other values are estimates.

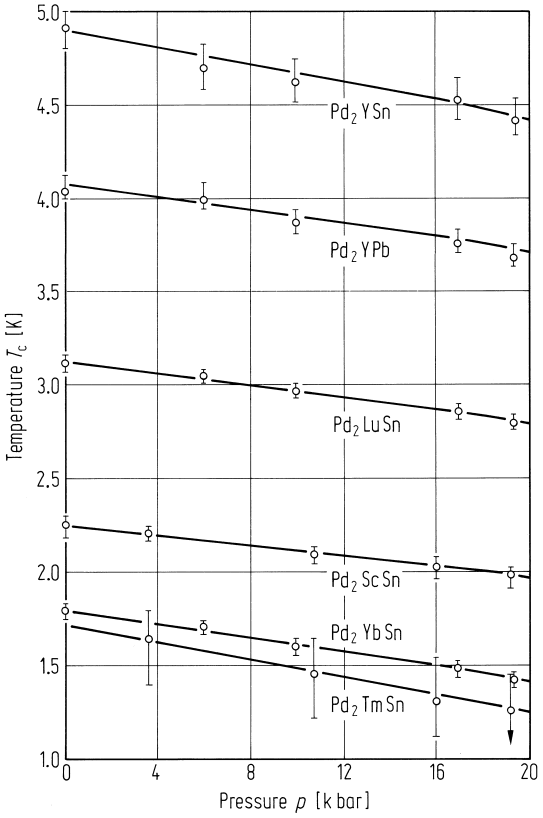

Fig. 332. Pressure dependence of the superconducting transition temperature T_c for Pd_2YSn compounds [84J1].

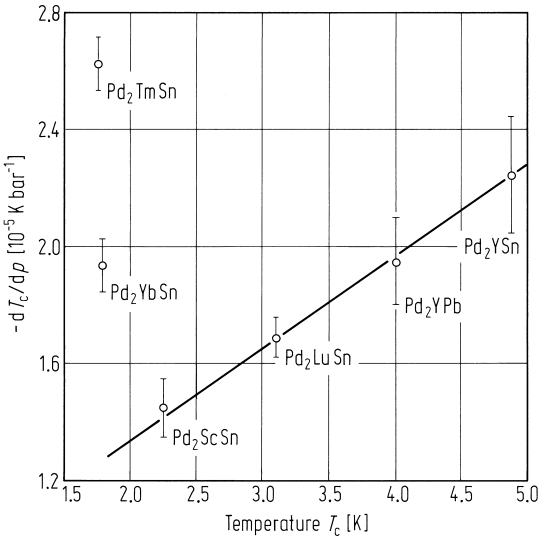

Fig. 334. Differential pressure dependence of the superconducting transition temperature T_c plotted against T_c for several palladium-tin based Heusler alloys [84J1].

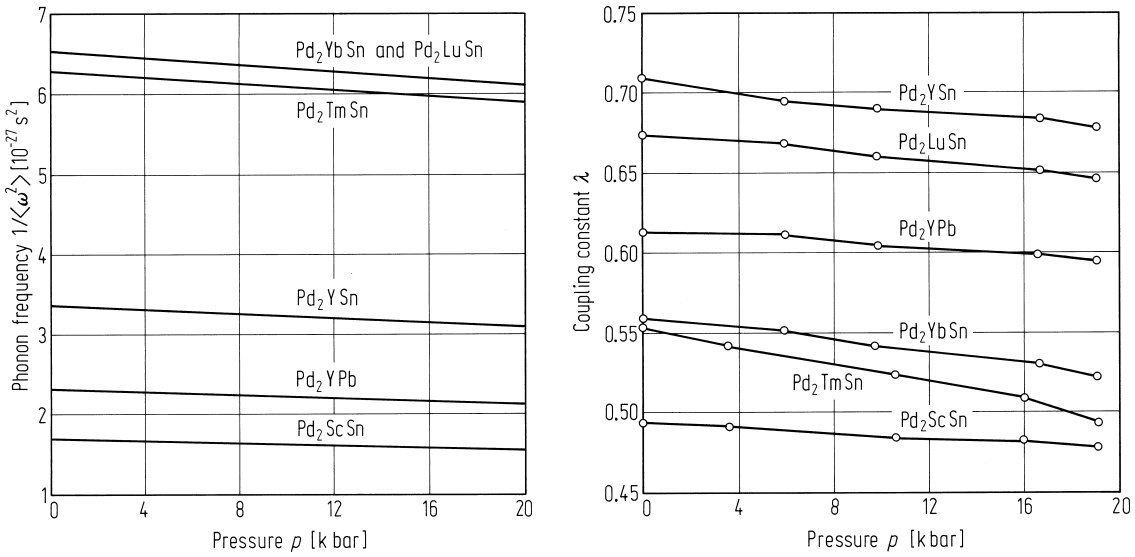

Fig. 333. Pressure dependence of the electron - phonon coupling constant λ and the inverse phonon frequency calculated in the strong coupling limit [84J1].

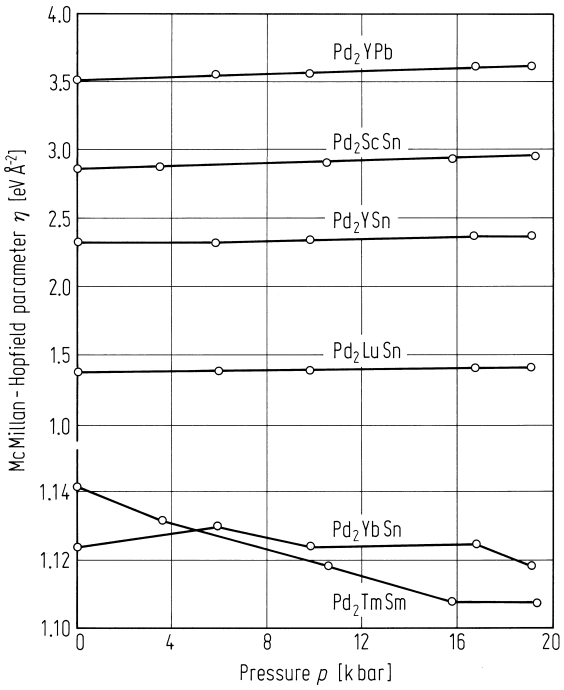

Fig. 335. Calculated pressure dependence of the McMillan-Hopfield parameter η. The insensitivity of η with respect to pressure indicates that the variation of T_c with pressure is due primarily to lattice stiffening [84J1].

1.5.5.7 Thermal properties

This section deals with the specific heat of Heuslers which do not become superconducting. Particular interest has been focused on compounds containing rare earth elements where the effects of the crystal field are important. Attention has also been concentrated on the possibility of discovering new Heavy Fermion systems. The data are analysed assuming electronic, phonon and nuclear contributions.